

Article

Surface Plasmon Waveguide Based on Nested Dielectric Parallel Nanowire Pairs Coated with Graphene

Lixia Yu ^{1,*}, Ji Liu ¹  and Wenrui Xue ² 

¹ School of Information and Communication Engineering, North University of China, Taiyuan 030051, China; liuji6@nuc.edu.cn

² College of Physics and Electronic Engineering, Shanxi University, Taiyuan 030006, China; wxue@sxu.edu.cn

* Correspondence: 20030675@nuc.edu.cn

Abstract: A kind of surface plasmon waveguide composed of two nested cylindrical dielectric parallel nanowire pairs coated with graphene was designed and studied. The dependence of the mode characteristics and the normalized gradient force of the lowest two modes supported by the waveguide on the parameters involved were analyzed by using the multipole method. To ensure rigor, the finite element method was employed to verify the accuracy of the multipole method, thus confirming its results. The results show that the multipole method is a powerful tool for handling this type of waveguide. The real part of the effective refractive index, the propagation length, the figure of merit, and the normalized gradient force can be significantly affected by the operating wavelength, the Fermi energy of graphene, the waveguide geometric parameters, and the refractive index of the inner dielectric nanowire. Due to the employment of nested dielectric nanowire pairs coated with graphene, this waveguide structure exhibits significant gradient force that surpasses $100 \text{ nN} \cdot \mu\text{m}^{-1} \cdot \text{mW}^{-1}$. The observed phenomena can be attributed to the interaction of the field with graphene. This waveguide holds promising potential for applications in micro/nano integration, optical tweezers, and sensing technologies.

Keywords: graphene; nanowire; waveguide; multipole method



Citation: Yu, L.; Liu, J.; Xue, W. Surface Plasmon Waveguide Based on Nested Dielectric Parallel Nanowire Pairs Coated with Graphene. *Photonics* **2024**, *11*, 441. <https://doi.org/10.3390/photonics11050441>

Received: 19 April 2024

Revised: 29 April 2024

Accepted: 7 May 2024

Published: 9 May 2024



Copyright: © 2024 by the authors. Licensee MDPI, Basel, Switzerland. This article is an open access article distributed under the terms and conditions of the Creative Commons Attribution (CC BY) license (<https://creativecommons.org/licenses/by/4.0/>).

1. Introduction

Surface plasmon polaritons (SPPs) are electromagnetic modes that arise at the metal-dielectric interface through the interaction of free electrons and photons [1]. Thanks to their ability to transcend the diffraction limit and possess robust local field enhancement properties, SPPs offer immense potential for applications in nanoscale optical information transmission and processing [2], ultra-sensitive biological detection [3], sensing [4], and novel light sources [5].

Surface plasmon waveguides (SPWs) are devices that guide the propagation of SPPs [6]. The materials used to construct SPWs include noble metals [7], semiconductors [8], and two-dimensional materials such as molybdenum disulfide [9] and graphene [10]. The typical structures of SPWs are strip type [11,12], slot type [13,14], wedge type [15,16], channel type [16,17], hybrid type [18], etc.

In the infrared-to-terahertz frequency regime, graphene has properties similar to metals, and SPPs can be excited on its surface. Graphene-coated dielectric nanowires are a new type of surface plasmon waveguide that emerged in recent years [19]. A cylindrical dielectric nanowire coated with single-layer graphene was designed by Y. Gao et al. The authors obtained a dispersion relationship of modes using a semi-analytical method, and the low-order modes supported by this waveguide were characterized [20,21]. J.-P. Liu and his colleagues devised a cylindrical dielectric nanowire featuring a double-layer structure clad in single-layer graphene. Employing the finite-difference time-domain method, they examined the low-order mode sustained by this waveguide. Furthermore, they highlighted

that mode properties can be fine-tuned by varying the waveguide's geometric factors and graphene's Fermi energy, as referenced in [22]. Research findings pertaining to cylindrical dielectric nanowires, utilizing a double-layer graphene structure, reveal that factors such as the Fermi energy of graphene, the separation between its inner and outer layers, and the radius of the dielectric nanowires within the core region significantly influence modal behavior [23]. Notably, it has been demonstrated that the inherent tradeoff between mode confinement and propagation loss can be overcome [24]. Furthermore, the long-range SPP (LRSP) mode exhibits both an extended propagation length and deep subwavelength constraints, marking a significant advancement in the field [25]. R. Xing and his team designed a cylindrical dielectric nanowire that was coated with multiple layers of graphene. The results indicate that this waveguide has a stronger confinement ability on the field than a nanowire waveguide coated with graphene with the same outer diameter [26]. The results of research on graphene-coated dielectric nanowires with substrates show that radiation leakage to the substrate can be effectively suppressed by the introduced buffer layer [27], the deep subwavelength plasmon mode with ultra-low loss can be supported [28], and a longer propagation length and a smaller mode area can be obtained simultaneously [29]. The characteristics of the six lowest-order surface plasmon modes have been studied [30]. A dual-multilayer nanoring waveguide configuration was introduced, and both surface plasmon modes and the augmentation of the gap field within the intervening space between these waveguides were examined [31]. S. Ye et al.'s research on graphene-coated hexagonal boron nitride nanowire pairs shows that this waveguide supports both the plasmon phonon polarization (SPP-HP) mode and the phonon polarization (PHP) mode [32]. The findings of research on dielectric nanowire pairs coated with graphene and equipped with a substrate reveal that mode characteristics can be efficiently tailored by altering the thickness of the substrate, as reported in [33]. Inserting a low-refractive index material layer between the nanowire and the substrate can compensate for the accompanying loss of the substrate, so that the mode's characteristics can be adjusted to achieve better performance [34].

Optical forces play an essential role in small-particle manipulations with broad applications in biology, chemistry, and physics [35–41]. It has been demonstrated that, in comparison to plasmonic metal-coated nanowire systems, the unique properties of graphene plasmons (GPs) enable significantly greater field enhancement, and the gradient force between the two nanowires can be as high as $20 \text{ nN} \cdot \mu\text{m}^{-1} \cdot \text{mW}^{-1}$ [30]. Therefore, it is reasonable to expect the existence of a strong gradient force within nanowire systems coated with graphene that are coupled together.

Our team's investigation into nested dielectric nanowire waveguides coated with single-layer graphene on both inner and outer surfaces has uncovered fascinating results. We found that the three lowest modes—mode 0, mode 1, and mode 2—can be effectively combined using the zero-order mode or/and the first-order modes of two individual nanowires. Notably, mode 0 exhibits a superior figure of merit and the most optimal performance among these modes within the relevant parameter range. Furthermore, the characteristics of these modes can be tailored by adjusting the waveguide's parameters, the working wavelength, and the Fermi energy of graphene [42,43].

Based on our previous work [43], here, we designed a new type of waveguide composed of nested dielectric parallel nanowire pairs coated with graphene. To our knowledge, this type of eccentric nested dielectric parallel nanowire pairs coated with graphene has not been studied previously. Using the multipole method (MPM), the dependence of the mode characteristics of the two lowest-order modes of this kind of waveguide on the operating wavelength, the Fermi energy of graphene, the geometric parameters, and the refractive index of the inner dielectric nanowire were analyzed. This type of waveguide has broad application prospects in fields such as micro/nano integration, optical tweezers, and sensing [44,45].

The content of this paper is arranged as follows: in the second part, the structure model and calculation method will be introduced in detail. The third part is the results and discussion. A detailed discussion is conducted on the phenomenon and reasons why the

mode characteristics of two modes vary with the working wavelength, the Fermi energy of graphene, the geometric parameters, and the refractive index of the inner dielectric nanowire. The last part is the summary.

2. Waveguide Structure and Calculation Method

The waveguide structure presented in this paper is depicted in Figure 1 and consists of four nested cylindrical dielectric parallel nanowires coated with graphene. The radii of the cylindrical nanowires are ρ_{10} , ρ_{20} , ρ_{30} , and ρ_{40} , respectively. Assume that the minimum distance between the surface of the embedded cylindrical nanowire and the surface of the parent cylindrical nanowire is s and the minimum distance between the outer surfaces of two parallel nanowires is d . The surfaces of the four cylindrical nanowires are coated with a single layer of graphene material, and the surface conductivity is σ_g . The refractive indices of the dielectrics in region I, region II, region III, and region IV are n_1 , n_2 , n_3 , and n_4 , respectively. Region V is the air background with a refractive index of $n_0 = 1.0$.

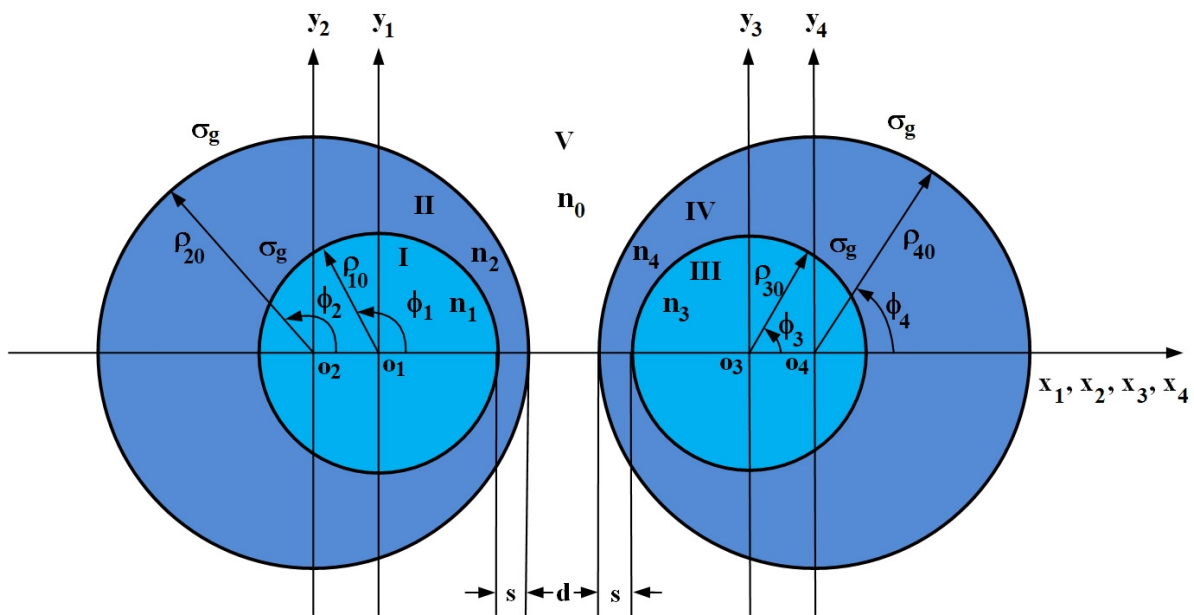


Figure 1. Cross-sectional view of a waveguide composed of two nested cylindrical dielectric parallel nanowires coated with graphene.

We use the multipole method to analyze the mode characteristics supported by this waveguide. The symmetric center o_i of the cylindrical nanowire is taken as the origin to establish a rectangular coordinate system $o_i - x_i y_i$ and a polar coordinate system $o_i - \rho_i \phi_i$. Here, $i = 1, 2, 3$, and 4 correspond to the four cylindrical nanowires shown in Figure 1, respectively. Assuming that the four cylindrical nanowires exist separately, the distribution of the E_z and H_z fields in their respective coordinate systems can be expanded into series. For example, for the first dielectric cylinder, they are as follows:

Inside the 1st cylindrical nanowire:

$$E_{z11}(\rho_1, \phi_1) = \sum_{m=0}^{\infty} A_m I_m(\lambda_1 \rho_1) \cos(m\phi_1) + \sum_{m=1}^{\infty} A'_m I_m(\lambda_1 \rho_1) \sin(m\phi_1) \quad (1)$$

$$H_{z11}(\rho_1, \phi_1) = \sum_{m=0}^{\infty} B_m I_m(\lambda_1 \rho_1) \cos(m\phi_1) + \sum_{m=1}^{\infty} B'_m I_m(\lambda_1 \rho_1) \sin(m\phi_1) \quad (2)$$

Outside the 1st cylindrical nanowire:

$$E_{z12}(\rho_1, \phi_1) = \sum_{m=0}^{\infty} C_m K_m(\lambda_2 \rho_1) \cos(m\phi_1) + \sum_{m=1}^{\infty} C'_m K_m(\lambda_2 \rho_1) \sin(m\phi_1) \quad (3)$$

$$H_{z12}(\rho_1, \phi_1) = \sum_{m=0}^{\infty} D_m K_m(\lambda_2 \rho_1) \cos(m\phi_1) + \sum_{m=1}^{\infty} D'_m K_m(\lambda_2 \rho_1) \sin(m\phi_1) \quad (4)$$

Here, I_m and K_m are Bessel functions of order m , and $A_m, A'_m, B_m,$ and B'_m are undetermined coefficients of order m . $\lambda_1 = \sqrt{\beta^2 - \omega^2 \varepsilon_1 \varepsilon_0 \mu_0}$, $\lambda_2 = \sqrt{\beta^2 - \omega^2 \varepsilon_2 \varepsilon_0 \mu_0}$. β is the propagation constant, $\varepsilon_1 = n_1^2$, $\varepsilon_2 = n_2^2$, ε_0 is the dielectric constant in vacuum, and μ_0 is the permeability in vacuum.

Utilizing the superposition principle of fields, the E_z and H_z field distributions can be derived individually in regions I, II, III, IV, and V. For example, in region I:

$$(E_z)_I = E_{z11}(\rho_1, \phi_1) + E_{z21}(\rho_2, \phi_2) + E_{z32}(\rho_3, \phi_3) + E_{z42}(\rho_4, \phi_4) \quad (5)$$

$$(H_z)_I = H_{z11}(\rho_1, \phi_1) + H_{z21}(\rho_2, \phi_2) + H_{z32}(\rho_3, \phi_3) + H_{z42}(\rho_4, \phi_4) \quad (6)$$

Here, $E_{z21}(\rho_2, \phi_2)$ and $H_{z21}(\rho_2, \phi_2)$ are the z component of the electric field strength and magnetic field strength inside the 2nd cylindrical nanowire, respectively. $E_{z32}(\rho_3, \phi_3)$ and $H_{z32}(\rho_3, \phi_3)$ are the z component of the electric field strength and magnetic field strength outside the 3rd cylindrical nanowire. $E_{z42}(\rho_4, \phi_4)$ and $H_{z42}(\rho_4, \phi_4)$ are the z component of the electric field strength and magnetic field strength outside the 4th cylindrical nanowire.

The distribution of transverse fields $(E_\rho)_i, (H_\rho)_i, (E_\phi)_i,$ and $(H_\phi)_i$ in regions i can be obtained by using the relationship between the transverse and longitudinal components of fields. Here $i = I, II, III, IV,$ and V . For example,

$$(E_\phi)_I = -\frac{1}{\lambda_1^2} \left\{ (-j\beta) \frac{1}{\rho_1} \left[\sum_{m=0}^{\infty} A_m I_m(\lambda_1 \rho_1) (-m) \sin(m\phi_1) + \sum_{m=0}^{\infty} A'_m I_m(\lambda_1 \rho_1) (m) \cos(m\phi_1) \right. \right. \\ \left. \left. + \frac{\partial}{\partial \phi_1} \left[\sum_{m=0}^{\infty} E_m I_m(\lambda_2 \rho_2) \cos(m\phi_2) + \sum_{m=1}^{\infty} E'_m I_m(\lambda_2 \rho_2) \sin(m\phi_2) \right] \right. \right. \\ \left. \left. + \frac{\partial}{\partial \phi_1} \left[\sum_{m=0}^{\infty} R_m K_m(\lambda_2 \rho_3) \cos(m\phi_3) + \sum_{m=1}^{\infty} R'_m K_m(\lambda_2 \rho_3) \sin(m\phi_3) \right] \right. \right. \\ \left. \left. + \frac{\partial}{\partial \phi_1} \left[\sum_{m=0}^{\infty} V_m K_m(\lambda_0 \rho_4) \cos(m\phi_4) + \sum_{m=1}^{\infty} V'_m K_m(\lambda_0 \rho_4) \sin(m\phi_4) \right] \right] \right. \\ \left. + (j\omega\mu_0) \left[\sum_{m=0}^{\infty} B_m(\lambda_1) I_m(\lambda_1 \rho_1) \cos(m\phi_1) + \sum_{m=0}^{\infty} B'_m(\lambda_1) I'_m(\lambda_1 \rho_1) \sin(m\phi_1) \right. \right. \\ \left. \left. + \frac{\partial}{\partial \rho_1} \left[\sum_{m=0}^{\infty} F_m I_m(\lambda_2 \rho_2) \cos(m\phi_2) + \sum_{m=1}^{\infty} F'_m I_m(\lambda_2 \rho_2) \sin(m\phi_2) \right] \right. \right. \\ \left. \left. + \frac{\partial}{\partial \rho_1} \left[\sum_{m=0}^{\infty} S_m K_m(\lambda_2 \rho_3) \cos(m\phi_3) + \sum_{m=1}^{\infty} S'_m K_m(\lambda_2 \rho_3) \sin(m\phi_3) \right] \right. \right. \\ \left. \left. + \frac{\partial}{\partial \rho_1} \left[\sum_{m=0}^{\infty} W_m K_m(\lambda_0 \rho_4) \cos(m\phi_4) + \sum_{m=1}^{\infty} W'_m K_m(\lambda_0 \rho_4) \sin(m\phi_4) \right] \right] \right\} \quad (7)$$

Here, E_m and E'_m are undetermined coefficients of field E_{z21} inside the 2nd cylindrical nanowire, F_m and F'_m are undetermined coefficients of field H_{z21} inside the 2nd cylindrical nanowire, R_m and R'_m are undetermined coefficients of field E_{z32} outside the 3rd cylindrical nanowire, S_m and S'_m are undetermined coefficients of field H_{z32} outside the 3rd cylindrical nanowire, V_m and V'_m are undetermined coefficients of field E_{z42} outside the 4th cylindrical nanowire, and W_m and W'_m are undetermined coefficients of field H_{z42} outside the 4th cylindrical nanowire, $\lambda_0 = \sqrt{\beta^2 - \omega^2 \varepsilon_0 \mu_0}$.

The derivatives involved in the above formula can be obtained by the point product of the gradient of a scalar field and the unit vector of the polar coordinate system. For example,

$$\frac{\partial \psi(\rho_2, \phi_2)}{\partial \rho_1} = \nabla \psi(\rho_2, \phi_2) \cdot \hat{\rho}_1 = \frac{\partial \psi(\rho_2, \phi_2)}{\partial \rho_2} \hat{\rho}_2 \cdot \hat{\rho}_1 + \frac{\partial \psi(\rho_2, \phi_2)}{\rho_2 \partial \phi_2} \hat{\phi}_2 \cdot \hat{\rho}_1 \quad (8)$$

$$\frac{\partial \psi(\rho_2, \phi_2)}{\rho_1 \partial \phi_1} = \nabla \psi(\rho_2, \phi_2) \cdot \hat{\phi}_1 = \frac{\partial \psi(\rho_2, \phi_2)}{\partial \rho_2} \hat{\rho}_2 \cdot \hat{\phi}_1 + \frac{\partial \psi(\rho_2, \phi_2)}{\rho_2 \partial \phi_2} \hat{\phi}_2 \cdot \hat{\phi}_1 \quad (9)$$

Here, $\psi(\rho_2, \phi_2)$ represents any function with ρ_2 and ϕ_2 as variables, such as $I_m(\lambda_2\rho_2) \cos(m\phi_2)$. $\hat{\rho}_1$ and $\hat{\phi}_1$ represent the two unit vectors in the polar coordinate system $o_1 - \rho_1\phi_1$, while $\hat{\rho}_2$ and $\hat{\phi}_2$ represent the two unit vectors in the polar coordinate system $o_2 - \rho_2\phi_2$.

The boundary value relation of the tangential field applies at the four interfaces which are located at ρ_{10} , ρ_{20} , ρ_{30} , and ρ_{40} , respectively. For example, at the interface of ρ_{10} ,

$$(E_z)_I|_{\rho_{10}} = (E_z)_{II}|_{\rho_{10}} \tag{10}$$

$$(E_\phi)_I|_{\rho_{10}} = (E_\phi)_{II}|_{\rho_{10}} \tag{11}$$

$$(H_z)_I|_{\rho_{10}} - (H_z)_{II}|_{\rho_{10}} = \sigma_g(E_\phi)_I|_{\rho_{10}} \tag{12}$$

$$(H_\phi)_I|_{\rho_{10}} - (H_\phi)_{II}|_{\rho_{10}} = -\sigma_g(E_z)_I|_{\rho_{10}} \tag{13}$$

Here, σ_g is the conductivity of graphene, which is obtained from the Cooper formula [46]. From the given formula, we can derive a system of linear algebraic equations:

$$\begin{bmatrix} a_{mn}(0,0) & a_{mn}(0,1) & \dots & a_{mn}(0,31) \\ a_{mn}(1,0) & a_{mn}(1,1) & \dots & a_{mn}(1,31) \\ \dots & \dots & \dots & \dots \\ a_{mn}(15,0) & a_{mn}(15,1) & \dots & a_{mn}(15,31) \end{bmatrix} \begin{bmatrix} [A] \\ [A'] \\ \dots \\ [H'] \end{bmatrix} = 0 \tag{14}$$

Here, $[A]$ is the column vector composed of undetermined coefficients A_0, A_1, \dots and A_{M-1} . In order to perform calculations on a computer, the infinite series shown in Formulas (1)–(4) must be truncated. Here, M is the maximum value of m . To ensure that the coefficient matrix in formula (14) is a square matrix, the maximum value of n must be $2M$. $[A']$, $[B]$, \dots and $[H']$ are constructed in the same way. $a_{mn}(i, j)$ is the submatrix of $m \times n$, for example,

$$a_{mn}(0,0) = I_m(\lambda_1\rho_{10}) \cos(m\phi_{1n}) \tag{15}$$

We found that as M gradually increases, calculation accuracy will gradually improve. When $M = 15$, the results obtained by the multipole method are very close to those obtained by the finite element method, and the relative error can reach the order of 10^{-4} . In the following calculations, we take $M = 15$.

Solving the linear algebraic equations (14) by the singular value decomposition (SVD) method [47], the characteristics of each mode can be obtained, including the field distribution, the real part of the effective refractive index $Re(n_{eff})$, which describes the amount of phase delay per unit length in the waveguide relative to the phase delay per unit length in vacuum [48], and the imaginary part of the effective refractive index $Im(n_{eff})$, which describes the loss of the waveguide structure [48]. Then, propagation length L_{prop} and the figure of merit (FOM) can be obtained: $L_{prop} = \lambda / \{4\pi Im(n_{eff})\}$ [49], $FOM = Re(n_{eff}) / Im(n_{eff})$ [50]. Here, L_{prop} is used to describe the propagation distance, and FOM is used to describe the quality of the modes. The gradient force along the x direction is evaluated by $F_x = \oint_{\Sigma} \vec{T} \cdot d\vec{\sigma} \cdot \hat{e}_x$; here, \vec{T} is the Maxwell Stress Tensor (MST), Σ is an arbitrary surface enclosing the left or the right nested cylindrical dielectric parallel nanowires, and \hat{e}_x is the unit vector along the x direction. The component of \vec{T} here is $T_{\alpha\beta} = \epsilon E_\alpha E_\beta + \mu H_\alpha H_\beta - \frac{1}{2} \delta_{\alpha\beta} (\epsilon E^2 + \mu H^2)$, where δ is the Kronecker delta function [51]. For the convenience of calculation, the gradient force F_x is normalized to f_x by the power along z direction, $f_x = F_x / \iint_{\Sigma'} S_z dx dy$, where S_z is the energy flow density component along the z direction of the mode and Σ' is the cross-section of the left or the right nested cylindrical dielectric parallel nanowire waveguide.

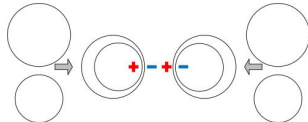
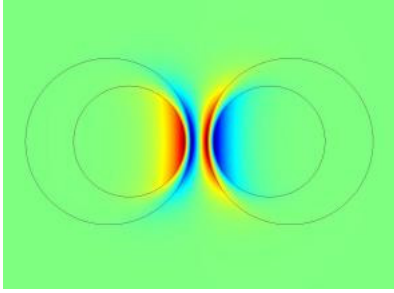
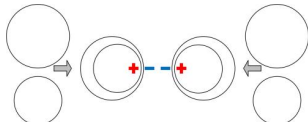
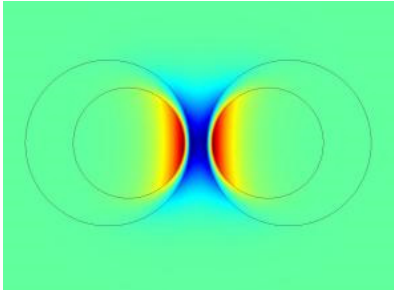
3. Results and Discussion

In this section, the synthesis of the two lowest-order modes supported by wave-guides is initially explored. Subsequently, the discussion focuses on how these modes' $Re(n_{eff})$, L_{prop} , FOM , and f_x vary with factors such as the working wavelength, the Fermi energy of graphene, the radii of embedded and parent cylindrical nanowires, and the minimum distances between the outer surfaces of parallel nanowires and between the surfaces of embedded and parent cylinders. For the sake of structural symmetry, it is assumed that the radii of two embedded cylindrical nanowires are the same, and the radii of the two parent cylindrical nanowires are also the same, i.e., $\rho_{10} = \rho_{30}$, $\rho_{20} = \rho_{40}$. The refractive indices of region I and region III are the same, while the refractive indices of region II and region IV are the same, i.e., $n_1 = n_3$, $n_2 = n_4$. To verify the accuracy of the multipole method, we also provide the results obtained by the finite element method. In the figures in Sections 3.2–3.8, solid lines represent the results obtained by the multipole method, and dotted lines represent the results obtained by the finite element method.

3.1. The Two Lowest-Order Modes

The waveguide shown in Figure 1 supports many modes. Table 1 shows the two lowest-order modes, namely, the combination of mode 0 and mode 1, the distribution of electric field z component, and the distribution of electric field intensity. From Table 1, it can be seen that mode 0 and mode 1 are combined by zero-order modes supported by a single nanowire [20,21]. The E_z field distribution of mode 0 is symmetric about the x-axis and antisymmetric about the y-axis, while the E_z field distribution of mode 1 is symmetric about both the x-axis and y-axis. Because the fields of these two modes are mainly concentrated in the gap area between the left and right embedded nanowires, they have a certain practical value, while the field distribution of other higher-order modes will diffuse to the entire range of the waveguide, which is less practical. Therefore, in the following text, we will only discuss the mode characteristics of the two lowest-order modes.

Table 1. Combination and the electric field component in the z direction of the two-lowest order modes.

Mode	Combination	E_z
0		
1		

3.2. Influence of the Working Wavelength on Mode Characteristics

Under the conditions of $E_f = 0.5$ eV, $\rho_{10} = \rho_{30} = 150$ nm, $\rho_{20} = \rho_{40} = 220$ nm, $s = 20$ nm, $d = 75$ nm, $n_1 = n_3 = 1.45$, and $n_2 = n_4 = 1.45$, the relationship of the real part of the effective refractive index, propagation length, figure of merit, and normalized gradient

force of the two modes with wavelength is shown in Figure 2a,b. It can be seen that in the wavelength range of 8–14 microns, as the wavelength increases, the $Re(n_{eff})$ of both modes monotonically decreases. Mode 0 has a slower descent speed, while mode 1 has a faster descent speed. The L_{prop} of the two modes shows a monotonic growth trend. The propagation distance of mode 0 and mode 1 is almost the same. FOM shows a trend of first increasing and then decreasing. Under certain wavelength conditions, mode 0 has a higher figure of merit and mode 1 has a lower figure of merit. The magnitude of the normalized gradient force f_x shows a monotonic decreasing trend. Mode 0 has a slower descent speed, while mode 1 has a faster descent speed. The above phenomenon can be explained by the fact that different wavelengths correspond to different field distributions of the mode. Figure 2c,d show the E_z field distribution of mode 1 at wavelengths of 8 microns and 14 microns, respectively. Comparing the two figures, it becomes evident that as the wavelength decreases, the field becomes more confined to the graphene layer adjacent to the surfaces of the two nanowires. This confinement enhances the interaction between the field and the graphene, leading to increased losses, shorter propagation distances, and stronger gradient forces. Conversely, when the wavelength increases, the field diffuses more widely into the space separating the nanowires, weakening the interaction with the graphene. Consequently, there is reduced loss, a longer propagation distance, and a weaker gradient force.

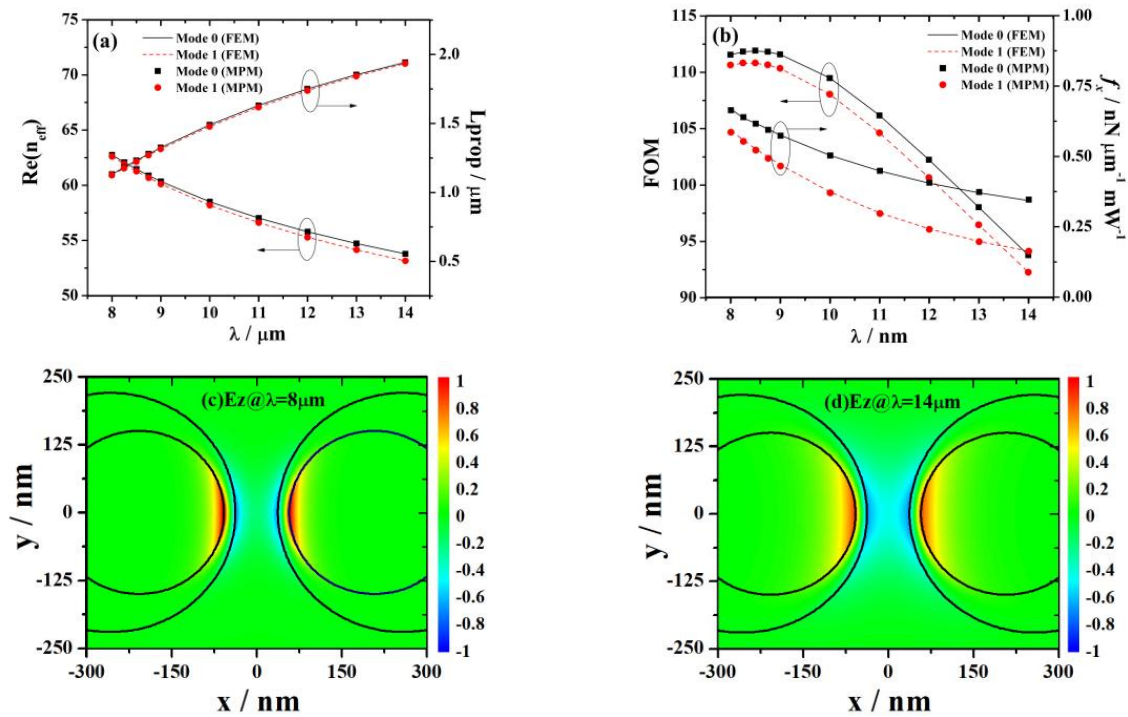


Figure 2. The dependence of $Re(n_{eff})$ and L_{prop} (a), FOM and f_x (b) on the working wavelength. The E_z field distribution of mode 1 at $\lambda = 8 \mu\text{m}$ (c) and $14 \mu\text{m}$ (d).

3.3. Influence of the Fermi Energy of Graphene on Mode Characteristics

The relationship between the real part of the effective refractive index, propagation length, figure of merit, and normalized gradient force of the two modes with Fermi energy under the conditions of $\lambda = 10 \mu\text{m}$, $\rho_{10} = \rho_{30} = 150 \text{ nm}$, $\rho_{20} = \rho_{40} = 220 \text{ nm}$, $s = 20 \text{ nm}$, $d = 75 \text{ nm}$, $n_1 = n_3 = 1.45$, and $n_2 = n_4 = 1.45$ is shown in Figure 3a,b. It can be seen that in the range of 0.2–1.2 eV, as the Fermi energy increases, the $Re(n_{eff})$ of both modes monotonically decreases. The descent speed of mode 0 is almost the same as that of mode 1. The L_{prop} of both modes shows a monotonic growth trend. The propagation distance of mode 0 and mode 1 is almost the same. The FOM of both modes shows a monotonic growth trend. Under certain wavelength conditions, mode 0 has a higher figure of merit

and mode 1 has a lower figure of merit. The magnitude of the normalized gradient force f_x shows a monotonic decreasing trend. Mode 0 has a slower descent speed, while mode 1 has a faster descent speed. The above phenomenon can be explained by the fact that different Fermi energies correspond to different field distributions of the mode. The E_z field distribution of mode 1 at Fermi energies of 0.2 eV and 1.2 eV are shown in Figure 3c,d. Comparing the two graphs, it becomes apparent that when the Fermi energy is low, the field is more concentrated within the graphene layer adjacent to the nanowire surface between the two nanowires. This strong interaction between the field and graphene leads to increased losses, shortened propagation distances, and a relatively large normalized gradient force. Conversely, at high Fermi energy, the field spreads out into the space between the nanowires, weakening the interaction with the graphene. Consequently, there are reduced losses, longer propagation distances, and a relatively smaller normalized gradient force.

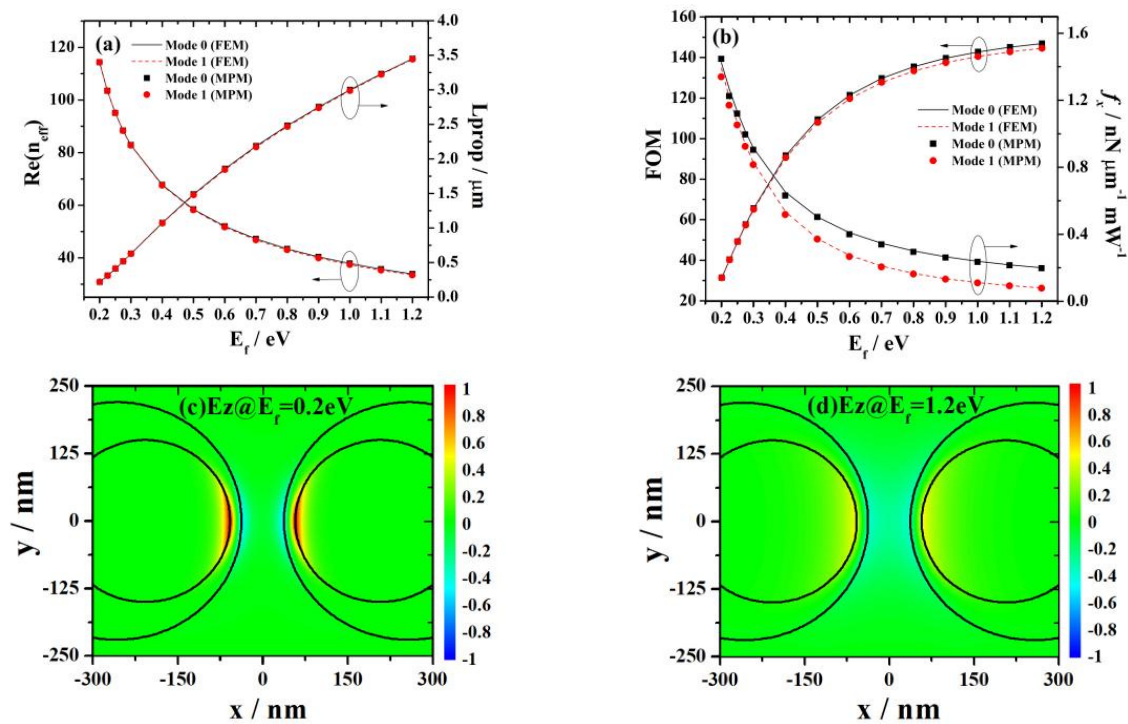


Figure 3. The dependence of $Re(n_{eff})$ and L_{prop} (a), FOM and f_x (b) on the Fermi energy of graphene. The E_z field distribution of mode 1 at $E_f = 0.2$ eV (c) and 1.2 eV (d).

3.4. Influence of the Radii of the First Nanowire on Mode Characteristics

Under the conditions of $\lambda = 10 \mu\text{m}$, $E_f = 0.5$ eV, $\rho_{20} = \rho_{40} = 220$ nm, $s = 20$ nm, $d = 75$ nm, $n_1 = n_3 = 1.45$, and $n_2 = n_4 = 1.45$, the relationship between the real part of the effective refractive index, propagation length, figure of merit, and normalized gradient force of the two modes with the radius ρ_{10} ($\rho_{30} = \rho_{10}$) of the embedded cylindrical nanowire are shown in Figure 4a,b. It can be seen that, in the range of 80–200 nm, as ρ_{10} increases, the $Re(n_{eff})$ of both modes shows a trend of first decreasing and then increasing. The L_{prop} of the two modes shows a monotonic upward trend. The FOM of both modes shows a monotonic growth trend. The magnitude of the normalized gradient force f_x first shows a slow decreasing trend, and then shows a significant decreasing trend around 200 nm. When ρ_{10} is small, the $Re(n_{eff})$, L_{prop} , FOM, and f_x of mode 0 are all higher than the $Re(n_{eff})$, L_{prop} , FOM, and f_x of mode 1. When ρ_{10} approaches 200 nm, the embedded cylindrical nanowires and the parent cylindrical nanowires tend to be coaxial. At this point, the $Re(n_{eff})$, L_{prop} , FOM, and f_x of both mode 0 and mode 1 tend to be consistent. The above phenomenon can be explained by the fact that different radii of embedded cylindrical nanowires correspond to different mode field distributions. The E_z field distribution of mode 1 at $\rho_{10} = 80$ nm and

200 nm are shown in Figure 4c,d, respectively. Comparing these two graphs, we observe that when ρ_{10} is small, the field remains confined to the graphene layer close to the surface of the two nanowires. This leads to a strong interaction between the field and graphene, causing higher losses, shorter propagation distances, and a relatively larger normalized gradient force. However, when ρ_{10} reaches 200 nm, field intensity weakens and distributes almost uniformly across the four graphene rings. Consequently, the interaction between the field and graphene becomes relatively weak, resulting in lower losses, longer propagation distances, and a smaller normalized gradient force.

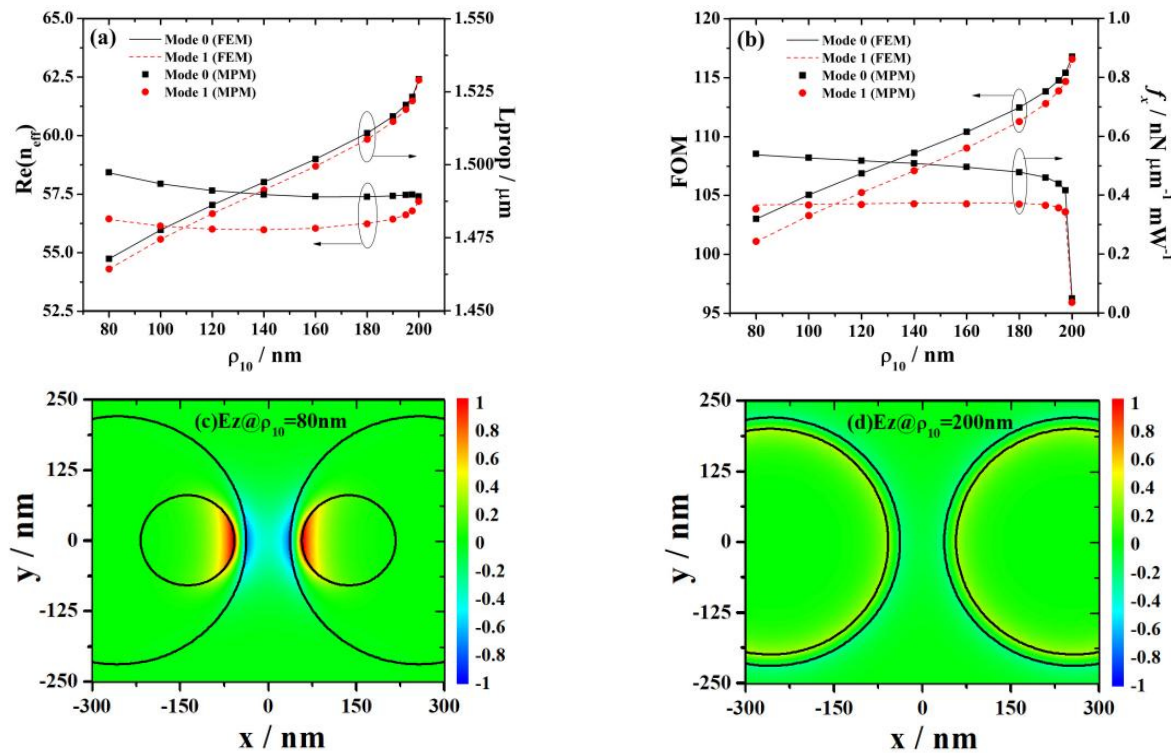


Figure 4. The dependence of $Re(n_{eff})$ and L_{prop} (a), FOM and f_x (b) on the radii of the 1st nanowire. The E_z field distribution of mode 1 at $\rho_{10} = 80$ nm (c) and 200 nm (d).

3.5. Influence of the Radii of the Second Nanowire on Mode Characteristics

The relationship between the real part of the effective refractive index, propagation length, figure of merit, and normalized gradient force of the two modes with the radius of the parent cylindrical nanowire ρ_{20} ($\rho_{40} = \rho_{20}$) under the conditions of $\lambda = 10 \mu m$, $E_f = 0.5$ eV, $\rho_{10} = \rho_{30} = 150$ nm, $s = 20$ nm, $d = 75$ nm, $n_1 = n_3 = 1.45$, and $n_2 = n_4 = 1.45$ is shown in Figure 5a,b. It can be seen that in the range of 170–230 nm, as ρ_{20} increases, the $Re(n_{eff})$, L_{prop} , and FOM of the two modes all show a monotonic decreasing trend, while the normalized gradient force f_x shows a monotonic increasing trend. When ρ_{20} is large, the $Re(n_{eff})$, L_{prop} , FOM, and f_x of mode 0 are all higher than the $Re(n_{eff})$, L_{prop} , FOM, and f_x of mode 1. When ρ_{20} approaches 170 nm, the embedded cylindrical nanowires and the parent cylindrical nanowires tend to be coaxial. At this time, the $Re(n_{eff})$, L_{prop} , FOM, and f_x of both mode 0 and mode 1 tend to be consistent. The above phenomenon can be explained by the fact that the radii of different parent cylindrical nanowires correspond to different mode field distributions. Figure 5c,d, respectively, show the E_z field distribution of mode 1 at $\rho_{20} = 170$ nm and 230 nm. Comparing the two graphs, it is evident that when ρ_{20} is small, the field spreads out into the gap between the two nanowires, weakening the interaction with the graphene. This leads to reduced losses and longer propagation distances. Conversely, as ρ_{20} increases, the field becomes more confined to the graphene layer adjacent to the nanowires' surfaces. This stronger interaction between the field and graphene results in greater losses and shorter propagation distances.

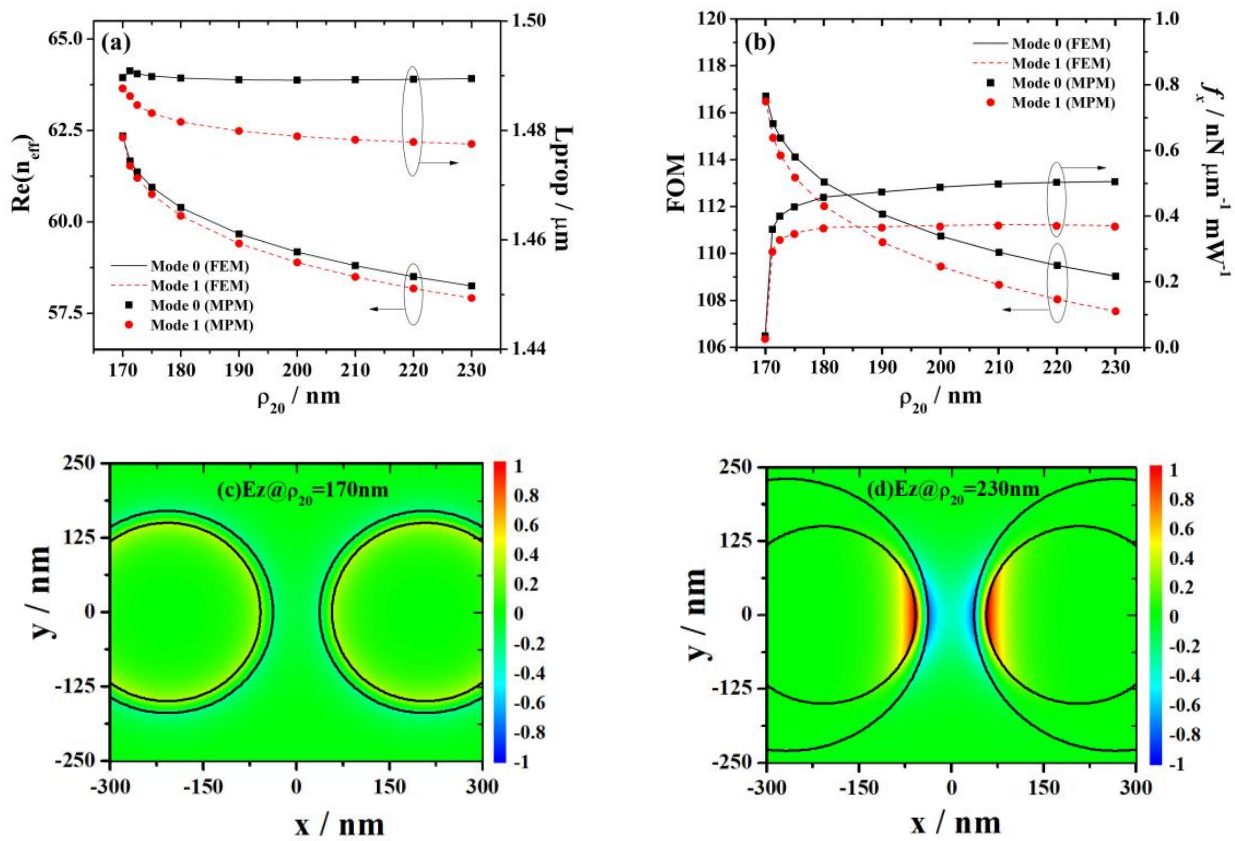


Figure 5. The dependence of $Re(n_{eff})$ and L_{prop} (a), FOM and f_x (b) on the radii of the 2nd nanowire. The E_z field distribution of mode 1 at $\rho_{20} = 170$ nm (c) and 230 nm (d).

3.6. Influence of the Minimum Distance between the Outer Surfaces of Two Parallel Nanowires on Mode Characteristics

The relationship between the real part of the effective refractive index, propagation length, figure of merit, and normalized gradient force of the two modes with a minimum distance between the outer surfaces of the two parallel nanowires under the conditions of $\lambda = 10 \mu\text{m}$, $E_f = 0.5 \text{ eV}$, $\rho_{10} = \rho_{30} = 150 \text{ nm}$, $\rho_{20} = \rho_{40} = 220 \text{ nm}$, $s = 20 \text{ nm}$, $n_1 = n_3 = 1.45$, and $n_2 = n_4 = 1.45$ is shown in Figure 6a,b. It can be seen that within the range of 10–105 nm, as d increases, the $Re(n_{eff})$ and f_x of mode 0 show a monotonic decreasing trend, while the $Re(n_{eff})$ and f_x of mode 1 show a monotonic increasing trend. The L_{prop} of mode 0 shows a monotonic upward trend, while the L_{prop} of mode 1 shows a monotonic downward trend. The FOM of mode 0 shows a monotonic decreasing trend, while the FOM of mode 1 shows first a decreasing and then an increasing trend. Under certain wavelength conditions, mode 0 has a higher figure of merit and mode 1 has a lower figure of merit. The above phenomenon can be explained by the fact that the radii of different parent cylindrical nanowires correspond to different mode field distributions. Figure 6c,d respectively show the E_z field distribution of mode 0 at $d = 10 \text{ nm}$ and 105 nm. Comparing the two graphs, it becomes apparent that as d decreases, field intensity is heightened and more focused on the graphene layer adjacent to the nanowires' surfaces. This stronger interaction between the field and graphene leads to increased losses, shorter propagation distances, and a stronger normalized gradient force. Conversely, when d is larger, the field intensity diminishes and slightly penetrates into the gap between the nanowires. As a result, the interaction with the graphene weakens, resulting in reduced losses, longer propagation distances, and a weaker normalized gradient force.

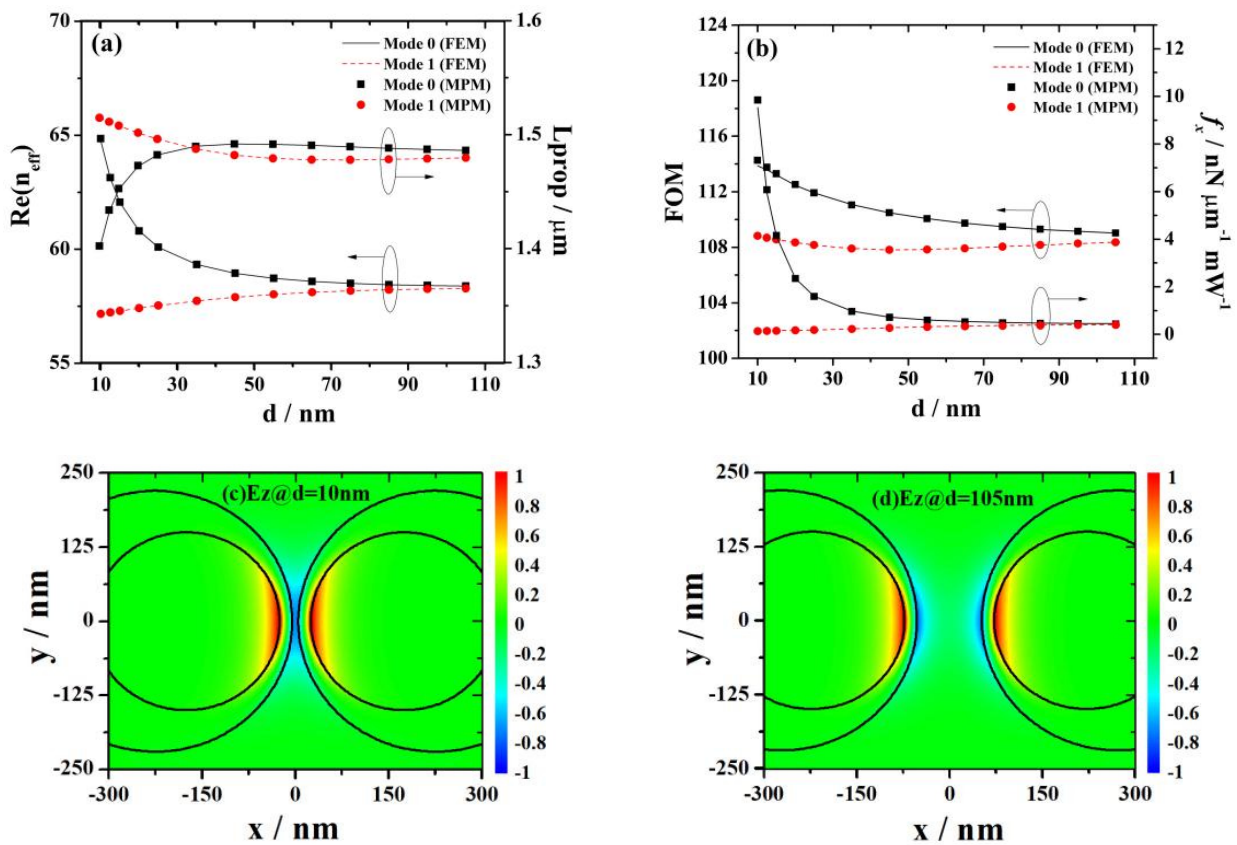


Figure 6. The dependence of $Re(n_{eff})$ and L_{prop} (a), FOM and f_x (b) on the minimum distance between the outer surfaces of two parallel nanowires. The E_z field distribution of mode 1 at $d = 10$ nm (c) and 105 nm (d).

3.7. Influence of the Minimum Distance between the Surface of the Embedded Cylinder and the Surface of the Parent Cylinder on Mode Characteristics

The relationship between the real part of the effective refractive index, propagation length, figure of merit, and normalized gradient force of the two modes with minimum spacing between the surface of the embedded cylindrical nanowire and the surface of the parent cylindrical nanowire under the conditions of $\lambda = 10 \mu\text{m}$, $E_f = 0.5 \text{ eV}$, $\rho_{10} = \rho_{30} = 150 \text{ nm}$, $\rho_{20} = \rho_{40} = 220 \text{ nm}$, $d = 75 \text{ nm}$, $n_1 = n_3 = 1.45$, and $n_2 = n_4 = 1.45$ is shown in Figure 7a,b. It can be seen that within the range of 10–70 nm, as s increases, the $Re(n_{eff})$, FOM, and f_x of the two modes all show a monotonic decreasing trend. Mode 0 has a slower descent speed, while mode 1 has a faster descent speed. The L_{prop} of the two modes shows a monotonic growth trend. Mode 0 has a faster growth rate, while mode 1 has a slower growth rate. The above phenomenon can be explained by the fact that the minimum spacing between the surfaces of different embedded cylindrical nanowires and the surfaces of the parent cylindrical nanowires corresponds to different mode field distributions. Figure 7c,d respectively show the E_z field distribution of mode 1 at $s = 10 \text{ nm}$ and 70 nm . Comparing the two graphs, it is evident that when s is small, the field is predominantly confined to the graphene layer adjacent to the nanowires' surfaces. This results in a stronger interaction between the field and graphene, leading to increased losses, shortened propagation distances, and a stronger normalized gradient force. However, when s is large, the field is primarily distributed in the background space separating the nanowires. Consequently, the interaction between the field and graphene is weaker, leading to reduced losses, longer propagation distances, and a weaker normalized gradient force.

conclusion applies to changing the Fermi energy of graphene, as shown in Figure 3a. In Figure 4a, it can be seen that the propagation distance of mode 0 and mode 1 is slightly different. The reason for this phenomenon is that, when the radius of the embedded nanowire is changed, the intensity and distribution range of the field distribution corresponding to mode 1 and mode 0 are slightly different, the interaction between graphene and the field is also slightly different, and the pace of change is also slightly different. Therefore, the variation of propagation distance with the radius of the embedded nanowire is also slightly different. The same conclusion applies to changing other geometric structural parameters, as shown in Figure 5a, Figure 6a, and Figure 7a.

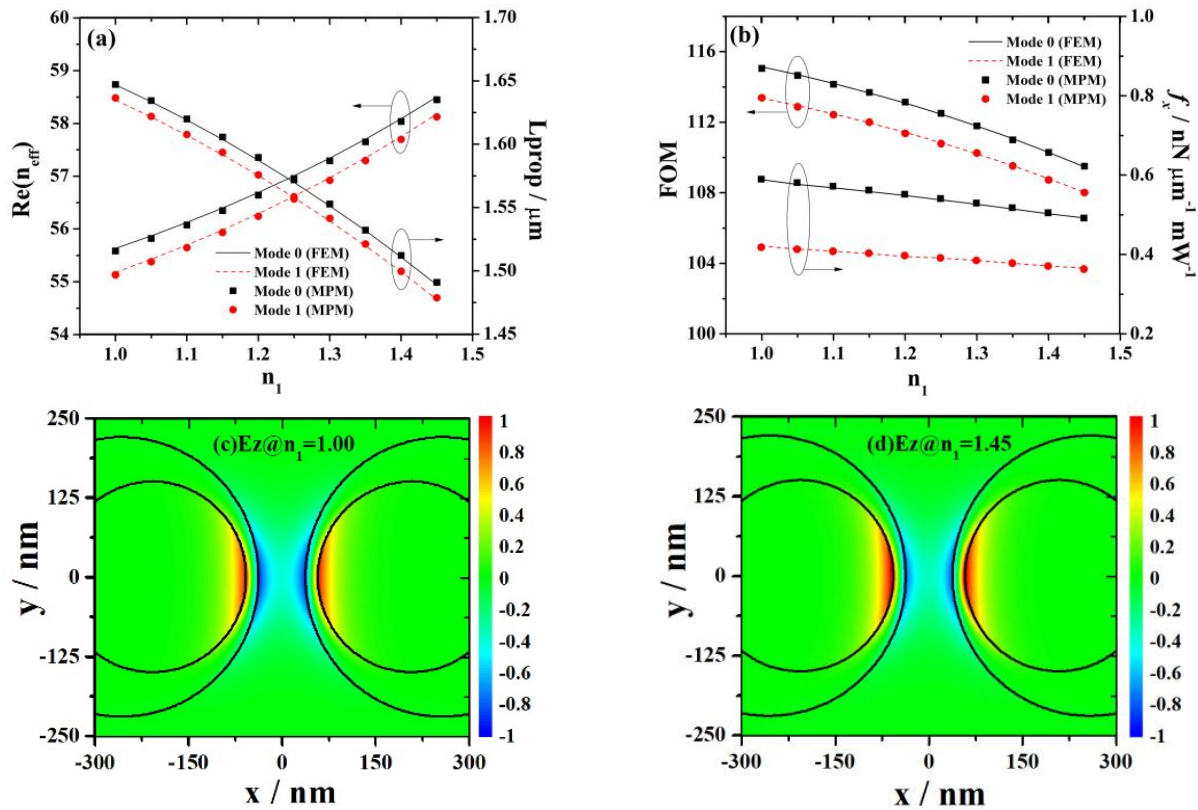


Figure 8. The dependence of $Re(n_{eff})$ and L_{prop} (a), FOM and f_x (b) on the refractive index of region I (or region III). The E_z field distribution of mode 1 at $n_1 = 1.00$ (c) and 1.45 nm (d).

The nested dielectric parallel nanowire pairs coated with graphene display a significant gradient force that surpasses $100 \text{ nN} \cdot \mu\text{m}^{-1} \cdot \text{mW}^{-1}$, as clearly demonstrated in Figure 5b, Figure 6b, Figure 7b, and Figure 8b. This result surpasses the findings reported in reference [30].

The multipole method is a semi-analytical method, while the finite element method is a numerical method. In terms of the physical mechanism of pattern formation, the multipole method is superior to the finite element method.

4. Conclusions

In this paper, a kind of waveguide consisting of four nested cylindrical dielectric parallel nanowires coated with graphene was designed, and characteristics of the lowest two modes supported by this waveguide were analyzed using the multipole method. In this method, the longitudinal components of the field are expanded firstly by the Bessel function in four cylindrical coordinate systems; then, the characteristic equation of the mode is obtained by virtue of the superposition principle of the field and the boundary value relationship, and the effective refractive index of the mode and the corresponding mode field distribution are finally obtained by means of the linear algebra method. The

obtained results of the multipole method have been confirmed by the finite element method. Assuming $\rho_{10} = \rho_{30}$, $\rho_{20} = \rho_{40}$, $n_1 = n_3$, and $n_2 = n_4$, we found that the $Re(n_{eff})$, L_{prop} , FOM , and f_x of the two lowest modes can be adjusted by adjusting λ , E_f , ρ_{10} , ρ_{20} , d , s , and n_1 . Utilizing a double-layer graphene structure, this waveguide demonstrates remarkable gradient forces, exceeding the performance of the comparable single-layer graphene structure. The various phenomena observed can be explained by the fact that different parameters correspond to different field distributions and different interactions between the field and graphene. The results of this article have certain theoretical guidance significance for the design, fabrication, and application of surface plasmon waveguides composed of nested parallel dielectric nanowire pairs with graphene coating.

Author Contributions: Investigation, writing—original draft preparation, L.Y.; validation, writing—review and editing, J.L.; methodology, software, supervision, W.X. All authors have read and agreed to the published version of the manuscript.

Funding: This research was funded by the Shanxi Scholarship Council of China, grant number 2023-141; the Fundamental Research Program of Shanxi Province, grant number 202103021224188, 202203021221101; and the Open Project of Key Laboratory, North University of China, grant number DXMBJJ2022-02.

Institutional Review Board Statement: Not applicable.

Informed Consent Statement: Not applicable.

Data Availability Statement: The data presented in this study are available on request from the corresponding author.

Acknowledgments: The authors thank Shanxi Cloud Era Technology Company Ltd. for its computing services for this work.

Conflicts of Interest: The authors declare no conflict of interest.

References

1. Khan, Q.; Khan, A.; Bacha, B.A.; Khan, M.; Khesro, A. Sensitivity of the surface plasmon polariton waves at the interface of metal and dielectric medium using doppler broadening effect. *Plasmonics* **2024**, *19*, 123–129. [[CrossRef](#)]
2. Xu, J.; Zhang, C.; Wang, Y.; Wang, M.; Xu, Y.; Wei, T.; Xie, Z.; Liu, S.; Lee, C.-K.; Hu, X.; et al. All-in-one, all-optical logic gates using liquid metal plasmon nonlinearity. *Nat. Commun.* **2024**, *15*, 1726. [[CrossRef](#)] [[PubMed](#)]
3. Zulfajri, M.; Gedda, G.; Ulla, H.; Habibati; Gollavelli, G.; Huang, G.G. A review on the chemical and biological sensing applications of silver/carbon dots nanocomposites with their interaction mechanisms. *Adv. Colloid Interface Sci.* **2024**, *325*, 103115. [[CrossRef](#)]
4. Vaidyanathan, A.; Mondal, B.; Rout, C.S.; Chakraborty, B. Plasmonic gas sensors based on nanomaterials: Mechanisms and recent developments. *J. Phys. D Appl. Phys.* **2024**, *57*, 263002. [[CrossRef](#)]
5. Ramírez, M.O.; Molina, P.; Hernández-Pinilla, D.; López-Polín, G.; Ares, P.; Lozano-Martín, L.; Yan, H.; Wang, Y.; Sarkar, S.; Al Shuhaib, J.H.; et al. Integrating 2D materials and plasmonics on Lithium Niobate platforms for pulsed laser operation at the nanoscale. *Laser Photonics Rev.* **2024**, *18*, 2300817. [[CrossRef](#)]
6. Fang, Y.; Sun, M. Nanoplasmonic waveguides: Towards applications in integrated nanophotonic circuits. *Light Sci. Appl.* **2015**, *4*, e294. [[CrossRef](#)]
7. Boltasseva, A.; Nikolajsen, T.; Leosson, K.; Kjaer, K.; Larsen, M.; Bozhevolnyi, S. Integrated optical components utilizing long-range surface plasmon polaritons. *J. Light. Technol.* **2005**, *23*, 413–422. [[CrossRef](#)]
8. Oulton, R.F.; Sorger, V.J.; Genov, D.A.; Pile, D.F.P.; Zhang, X. A hybrid plasmonic waveguide for subwavelength confinement and long-range propagation. *Nat. Photonics* **2008**, *2*, 496–500. [[CrossRef](#)]
9. Kuppaddakkath, A.; Najafidehaghani, E.; Gan, Z.; Tuniz, A.; Ngo, G.Q.; Knopf, H.; Löchner, F.J.F.; Abtahi, F.; Bucher, T.; Shradha, S.; et al. Direct growth of monolayer MoS₂ on nanostructured silicon waveguides. *Nanophotonics* **2022**, *11*, 4397–4408. [[CrossRef](#)]
10. Liu, Z.; Yang, C.; Wan, P.; Ding, L.; Xu, W. Dielectric-loaded black phosphorus surface plasmon polariton waveguides. *Opt. Express* **2019**, *27*, 18005–18015. [[CrossRef](#)]
11. Berini, P. Plasmon–polariton modes guided by a metal film of finite width. *Opt. Lett.* **1999**, *24*, 1011–1013. [[CrossRef](#)]
12. Nikitin, A.Y.; Guinea, F.; Garcia-Vidal, F.J.; Martín-Moreno, L. Edge and waveguide terahertz surface plasmon modes in graphene microribbons. *Phys. Rev. B* **2011**, *84*, 161407. [[CrossRef](#)]
13. Liu, L.; Han, Z.; He, S. Novel surface plasmon waveguide for high integration. *Opt. Express* **2005**, *13*, 6645–6650. [[CrossRef](#)]
14. He, S.; Zhang, X.; He, Y. Graphene nano-ribbon waveguides of record small mode area and ultra-high effective refractive indices for future VLSI. *Opt. Express* **2013**, *21*, 30664–30673. [[CrossRef](#)] [[PubMed](#)]

15. Pile, D.F.P.; Ogawa, T.; Gramotnev, D.K.; Okamoto, T.; Haraguchi, M.; Fukui, M.; Matsuo, S. Theoretical and experimental investigation of strongly localized plasmons on triangular metal wedges for subwavelength waveguiding. *Appl. Phys. Lett.* **2005**, *87*, 061106. [[CrossRef](#)]
16. Liu, P.; Zhang, X.; Ma, Z.; Cai, W.; Wang, L.; Xu, J. Surface plasmon modes in graphene wedge and groove waveguides. *Opt. Express* **2013**, *21*, 32432–32440. [[CrossRef](#)] [[PubMed](#)]
17. Gramotnev, D.K.; Pile, D.F.P. Single-mode subwavelength waveguide with channel plasmon-polaritons in triangular grooves on a metal surface. *Appl. Phys. Lett.* **2004**, *85*, 6323–6325. [[CrossRef](#)]
18. Dai, D.; He, S. A silicon-based hybrid plasmonic waveguide with a metal cap for a nano-scale light confinement. *Opt. Express* **2009**, *17*, 16646–16653. [[CrossRef](#)]
19. Saeed, M.; Ghaffar, A.; Rehman, S.; Naz, M.Y.; Shukrullah, S.; Naqvi, Q.A. Graphene-based plasmonic waveguides: A mini review. *Plasmonics* **2022**, *17*, 901–911. [[CrossRef](#)]
20. Gao, Y.; Ren, G.; Zhu, B.; Wang, J.; Jian, S. Single-mode graphene-coated nanowire plasmonic waveguide. *Opt. Lett.* **2014**, *39*, 5909–5912. [[CrossRef](#)]
21. Gao, Y.; Ren, G.; Zhu, B.; Liu, H.; Lian, Y.; Jian, S. Analytical model for plasmon modes in graphene-coated nanowire. *Opt. Express* **2014**, *22*, 24322–24331. [[CrossRef](#)]
22. Liu, J.P.; Zhai, X.; Wang, L.L.; Li, H.-J.; Xie, F.; Lin, Q.; Xia, S.-X. Analysis of mid-infrared surface plasmon modes in a graphene-based cylindrical hybrid waveguide. *Plasmonics* **2016**, *11*, 703. [[CrossRef](#)]
23. Yang, J.F.; Yang, J.J.; Deng, W.; Mao, F.; Huang, M. Transmission properties and molecular sensing application of CGPW. *Opt. Express* **2015**, *23*, 32289–32299. [[CrossRef](#)]
24. Zhao, T.; Hu, M.; Zhong, R.; Chen, X.; Zhang, P.; Gong, S.; Zhang, C.; Liu, S. Plasmon modes of circular cylindrical doublelayer graphene. *Opt. Express* **2016**, *24*, 20461–20471. [[CrossRef](#)]
25. Liu, J.P.; Zhai, X.; Xie, F.; Wang, L.-L.; Xia, S.-X.; Li, H.-J.; Luo, X.; Shang, X.-J. Analytical model of mid-infrared surface plasmon modes in a cylindrical long-range waveguide with double-layer graphene. *J. Light. Technol.* **2017**, *35*, 1971–1979. [[CrossRef](#)]
26. Xing, R.; Jian, S. Numerical analysis on tunable multilayer nanoring waveguide. *IEEE Photonics Technol. Lett.* **2017**, *29*, 967–970. [[CrossRef](#)]
27. Hajati, M.; Hajati, Y. High-performance and low-loss plasmon waveguiding in graphene-coated nanowire with substrate. *J. Opt. Soc. Am. B* **2016**, *33*, 2560. [[CrossRef](#)]
28. Teng, D.; Wang, K.; Huan, Q.; Chen, W.; Li, Z. High-performance light transmission based on graphene plasmonic waveguides. *J. Mater. Chem. C* **2020**, *8*, 6832–6838. [[CrossRef](#)]
29. Teng, D.; Yang, Y.; Guo, J.; Ma, W.; Tang, Y.; Wang, K. Efficient guiding mid-infrared waves with graphene-coated nanowire based plasmon waveguides. *Results Phys.* **2020**, *17*, 103169. [[CrossRef](#)]
30. Zhu, B.; Ren, G.; Yang, Y.; Gao, Y.; Wu, B.; Lian, Y.; Wang, J.; Jian, S. Field enhancement and gradient force in the graphene-coated nanowire pairs. *Plasmonics* **2015**, *10*, 839–845. [[CrossRef](#)]
31. Xing, R.; Jian, S. Numerical analysis on the multilayer nanoring waveguide pair. *IEEE Photonics Technol. Lett.* **2016**, *28*, 2779–2782. [[CrossRef](#)]
32. Ye, S.; Wang, Z.; Sun, C.; Dong, C.; Wei, B.; Wu, B.; Jian, S. Plasmon-phonon-polariton modes and field enhancement in the graphene-coated hexagon boron nitride nanowire pairs. *Opt. Express* **2018**, *26*, 23854–23867. [[CrossRef](#)] [[PubMed](#)]
33. Hajati, M.; Hajati, Y. Plasmonic characteristics of two vertically coupled graphene-coated nanowires integrated with substrate. *Appl. Opt.* **2017**, *56*, 870–875. [[CrossRef](#)]
34. Teng, D.; Wang, K.; Huan, Q.; Zhao, Y.; Tang, Y. High-performance transmission of surface plasmons in graphene-covered nanowire pairs with substrate. *Nanomaterials* **2019**, *9*, 1594. [[CrossRef](#)] [[PubMed](#)]
35. Kotsifaki, D.G.; Chormaic, S.N. Plasmonic optical tweezers based on nanostructures: Fundamentals, advances and prospects. *Nanophotonics* **2019**, *8*, 1227–1245. [[CrossRef](#)]
36. Tan, H.; Hu, H.; Huang, L.; Qian, K. Plasmonic tweezers for optical manipulation and biomedical applications. *Analyst* **2020**, *145*, 5699–5712. [[CrossRef](#)]
37. Hu, S.; Liao, Z.W.; Cai, L.; Jiang, X.X. Near-field optical tweezers for chemistry and biology. *Phys. Status Solidi A* **2020**, *217*, 1900604. [[CrossRef](#)]
38. Li, H.; Cao, Y.; Zhou, L.; Xu, X.; Zhu, T.; Shi, Y.; Qiu, C.-W.; Ding, W. Optical pulling forces and their applications. *Adv. Opt. Photonics* **2020**, *12*, 288–366. [[CrossRef](#)]
39. Zhang, Y.; Min, C.; Dou, X.; Wang, X.; Urbach, H.P.; Somekh, M.G.; Yuan, X. Plasmonic tweezers: For nanoscale optical trapping and beyond. *Light Sci. Appl.* **2021**, *10*, 59. [[CrossRef](#)]
40. Zhou, L.M.; Shi, Y.; Zhu, X.; Hu, G.; Cao, G.; Hu, J.; Qiu, C.-W. Recent progress on optical micro/nanomanipulations: Structured forces, structured particles, and synergetic applications. *ACS Nano* **2022**, *16*, 13264–13278. [[CrossRef](#)]
41. Samadi, M.; Alibeigloo, P.; Aqhili, A.; Khosravi, M.A.; Saeidi, F.; Vasini, S.; Ghorbanzadeh, M.; Darbari, S.; Moravvej-Farshi, M.K. Plasmonic tweezers: Towards nanoscale manipulation. *Opt. Lasers Eng.* **2022**, *154*, 107001. [[CrossRef](#)]
42. Li, H.; Xue, W.; Li, N.; Du, Y.; Li, C. Mode characteristics of a graphene-coated cylindrical dielectric waveguide with a nested eccentric hollow elliptical cylinder. *J. Opt. Soc. Am. B* **2022**, *39*, 2944–2956. [[CrossRef](#)]
43. Liu, J.; Yu, L.X.; Xue, W.R. Mode characteristics of nested eccentric waveguides constructed by two cylindrical nanowires coated with graphene. *Chin. Phys. B* **2022**, *31*, 036803. [[CrossRef](#)]

44. Teng, D.; Wang, K.; Li, Z. Graphene-coated nanowire waveguides and their applications. *Nanomaterials* **2020**, *10*, 229. [[CrossRef](#)]
45. Rezzouk, Y.; Khattou, S.; Amrani, M.; Noual, A.; El Boudouti, E.H.; Talbi, A.; Djafari-Rouhani, B. Bound states in the continuum and induced resonances in a simple plasmonic waveguide with sensing application. *Photonics* **2023**, *10*, 1284. [[CrossRef](#)]
46. Nikitin, A.Y.; Guinea, F.; Garcia-Vidal, F.J.; Martin-Moreno, L. Fields radiated by a nanoemitter in a graphene sheet. *Phys. Rev. B* **2011**, *84*, 195446. [[CrossRef](#)]
47. Golub, G.; van Loan, C.F. *Matrix Computations*, 4th ed.; The Johns Hopkins University Press: Baltimore, MD, USA, 2013.
48. Teng, D.; Wang, K.; Li, Z.; Zhao, Y. Graphene-coated nanowire dimers for deep subwavelength waveguiding in mid-infrared range. *Opt. Express* **2019**, *27*, 12458–12469. [[CrossRef](#)]
49. He, X.Q.; Ning, T.G.; Pei, L.; Zheng, J.J.; Li, J.; Wen, X.D. Tunable hybridization of graphene plasmons and dielectric modes for highly confined light transmit at terahertz wavelength. *Opt. Express* **2019**, *27*, 5961–5972. [[CrossRef](#)]
50. Hajati, M.; Hajati, Y. Deep subwavelength confinement of mid-infrared plasmon modes by coupling graphene-coated nanowire with a dielectric substrate. *Plasmonics* **2018**, *13*, 403–412. [[CrossRef](#)]
51. Novotny, L.; Hecht, B. *Principles of Nano-Optics*, 2nd ed.; Cambridge University Press: Cambridge, UK, 2012.

Disclaimer/Publisher’s Note: The statements, opinions and data contained in all publications are solely those of the individual author(s) and contributor(s) and not of MDPI and/or the editor(s). MDPI and/or the editor(s) disclaim responsibility for any injury to people or property resulting from any ideas, methods, instructions or products referred to in the content.